Voltage and Current Regulators Design of Power Converters in Islanded Microgrids based on State Feedback Decoupling

Federico, de Bosio; de Sousa Ribeiro, Luiz Antonio ; Freijedo Fernandez, Francisco Daniel; Guerrero, Josep M.; Pastorelli, Michele

Published in:
Proceedings of 8th IEEE Energy Conversion Congress and Exposition, 2016: ECCE 2016

DOI (link to publication from Publisher):
10.1109/ECCE.2016.7855559

Publication date:
2016

Document Version
Early version, also known as pre-print

Voltage and Current Regulators Design of Power Converters in Islanded Microgrids based on State Feedback Decoupling

Federico de Bosio[1], Luiz A. de S. Ribeiro[2], Francisco D. Freijedo[3], Josep M. Guerrero[4], Michele Pastorelli[1]
[1]Energy Department, Politecnico di Torino, 10129 Torino, Italy
[2]Institute of Electrical Energy, Federal University of Maranhao, 65072010 Sao Luis MA, Brazil
[3]Power Electronics Lab, École Polytechnique Fédérale de Lausanne, 1015 Lausanne, Vaud, Switzerland
[4]Department of Energy Technology, Aalborg University, 9200 Aalborg, Denmark www.microgrids.et.aau.dk

***Abstract*—In stand-alone microgrids based on voltage source inverters state feedback coupling between the capacitor voltage and inductor current degrades significantly the dynamics performance of voltage and current regulators. The decoupling of the controlled states is proposed, considering the limitations introduced by system delays. Moreover, a proportional resonant voltage controller is designed according to Nyquist criterion taking into account application requirements. Experimental tests performed in compliance with the UPS standards verify the theoretical analysis.**

***Index Terms*—Control system analysis, current control, microgrids, power quality, voltage control**

I. Introduction

THE dynamics performance of voltage and current regulators for islanded power systems is an essential factor considering the increasing share of renewable energy sources interfaced via power converters. In particular, the performance of the hierarchical control system of a microgrid [1] can degrade significantly if the inner loops at primary level have poor dynamics or interfere with outer loops with narrower bandwidths. This is the case in droop-controlled microgrids with secondary and tertiary control loops, as well as in variable speed drives [2]. Independently of the application, the design of the regulators should accomplish the main following tasks: i) to provide zero steady-state error; ii) to track the command reference, rejecting any disturbance within the controller bandwidth; iii) to have a bandwidth as wider as possible.

The use of Proportional Resonant (PR) controllers allows the implementation of the control laws in the αβ stationary reference frame. The features of this structure are equivalent to two PIs controllers implemented in two synchronous reference frames [3], one for the positive sequence and another for the negative sequence component of the signal. The advantage of using PR controllers stands in the low computational effort which depends on the low number of transformations required to reach the αβ stationary reference frame. In particular, this is an important feature for implementation in low-cost DSP units. Independently of the controller structure the effect of delays and voltage coupling should be carefully considered in the design stage.

Substantial research activities have been made in the design of regulators for systems with a strong electromotive force (e.g. grid connected and drives applications). However, design issues for stand-alone microgrids have not been so far discussed in depth. In this context, as proved in a recent publication [4], the coupling between the capacitor voltage and inductor current in VSI with LC output filter plays an important role in the performance of the inner regulators.

In the following, some relevant papers are analyzed, with special focus on stand-alone applications. In [5] an analytical method to determine the best possible gains of linear ac current controllers is derived, considering computation and PWM delays. In [6] different multi-loop control approaches using alternative feedback control variables are investigated. In [7] a methodology to assess the transient response of PR current regulators is proposed, aimed to achieve fast and non-oscillating transient responses in grid-connected applications. Recently, a fast acting current control scheme to regulate the load current during all energizing conditions of multiple load transformers powered by a UPS system has been proposed [8]. However, in general in the papers addressed, the effect of the delays for islanded systems have not been fully analyzed.

This paper addresses the abovementioned issues associated to islanded systems. This work is organized as follows. Firstly, the inner loop current control with and without state feedback voltage decoupling is analyzed. Subsequently, a PR voltage controller design is proposed. Detailed design and tuning is provided according to Nyquist criterion. The theoretical solution is supported by experimental results, according to the IEC 62040 standard for UPS systems.

II. System Description

In islanded microgrids the Voltage Source Inverter (VSI) is equipped with an LC filter at its output. In general, it operates in voltage control mode with the capacitor voltage and inductor currents being the controlled states. The block diagram including a three-phase three-legs inverter with its internal loops is presented in Fig. 1. The goal of the inner current loop is to track the commands from the outer voltage loop and to ensure disturbance rejection within its bandwidth.

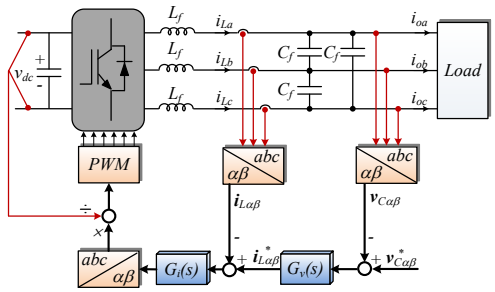

Fig. 1. Block diagram of a three phase VSI with voltage and current loops

The simplified block diagram of the closed-loop system is shown in Fig. 2, where $\boldsymbol{V}^*_{c\alpha\beta}$ and $\boldsymbol{I}^*_{L\alpha\beta}$ are the reference voltage and current vectors and $\boldsymbol{I}_{o\alpha\beta}$ is the output current vector, which acts as a disturbance to the system. $G_i(s)$ and $G_v(s)$ represent the current and voltage regulators transfer functions (TF), $G_{pwm}(s)$ is the TF related to computation and PWM delays, whereas $G_{dec}(s)$ is the TF related to the decoupling of the controlled states, designed to compensate for the system delay within the current controller bandwidth.

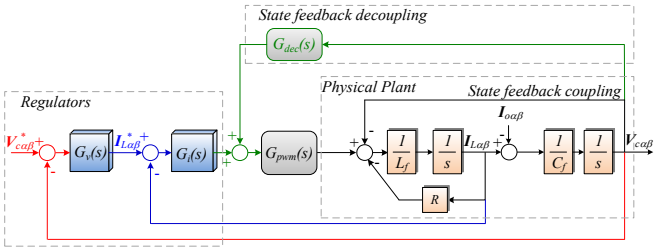

Fig. 2. Simplified block diagram of the closed-loop system

III. Current Regulator Design

The proportional gain of the current regulator k_{pI} is selected to achieve the desired bandwidth (f_{bw}), which has to be much wider than the outer loops [9]. A first order Padé approximation of the type $e^{-T_d s} \cong [1-(T_d/2)s]/[1+(T_d/2)s]$ is used to model the computation and PWM delays, where $T_d = 1.5/f_s$, being f_s the switching frequency. The system and current control parameters used both in the simulation and in laboratory tests are presented in Table I and Table II. The proportional gains of the current regulator are designed for amost the same bandwidth.

TABLE I
System Parameters

Parameter	Value
Switching frequency	$f_s = 10\ kHz$
Filter inductance	$L_f = 1.8\ mH$
Filter capacitor	$C_f = 27\ \mu F$
Inductor ESR	$R = 0.1\ \Omega$
Linear load	$R_l = 68\ \Omega$
Non linear load	$C_{NL} = 235\ \mu F$
	$R_{NL} = 184\ \Omega$
	$L_{NL} = 0.084\ mH$

TABLE II
Current Regulator Parameters

Parameter	Value
Proportional gain w/o decoupling	$k_{pI} = 5.61$
Proportional gain with decoupling	$k_{pI} = 6.42$

A P controller is considered as regulator for the current loop, i.e. $G_i(s) = k_{pI}$. With reference to Fig. 2, the transfer function (TF) of the system is

$$\boldsymbol{I}_{L\alpha\beta}(s) = \frac{G_i(s)G_{PWM}(s)C_f s}{a_1 s^2 + b_1 s + c_1}\boldsymbol{I}^*_{L\alpha\beta}(s) - \frac{G_{dec}(s)G_{PWM}(s) - 1}{a_1 s^2 + b_1 s + c_1}\boldsymbol{I}_{o\alpha\beta}(s), \quad (1)$$

being

$$a_1 = L_f C_f^2,$$
$$b_1 = RC_f + G_i(s)G_{PWM}(s)C_f,$$
$$c_1 = 1 - G_{dec}(s)G_{PWM}(s).$$

If the controlled states are coupled, i.e. $G_{dec}(s) = 0$, (1) becomes

$$\boldsymbol{I}_{L\alpha\beta}(s) = \frac{G_i(s)G_{PWM}(s)C_f s}{a_1 s^2 + b_1 s + 1}\boldsymbol{I}^*_{L\alpha\beta}(s) + \frac{1}{a_1 s^2 + b_1 s + 1}\boldsymbol{I}_{o\alpha\beta}(s). \quad (2)$$

Neglecting $\boldsymbol{I}_{o\alpha\beta}(s)$ in (2) results in the analysis of the tracking performance. Moreover, if the computation and PWM delays are neglected, i.e. $G_{PWM}(s) = 1$, (2) becomes

$$\boldsymbol{I}_{L\alpha\beta}(s) = \frac{G_i(s)C_f s}{L_f C_f^2 s^2 + (RC_f + G_i(s)C_f)s + 1}\boldsymbol{I}^*_{L\alpha\beta}(s). \quad (3)$$

It can be noticed from the root locus in Fig. 4 that as the gain is increased, higher damping is achieved. This is in contrast with the results where system delays are included for analysis.

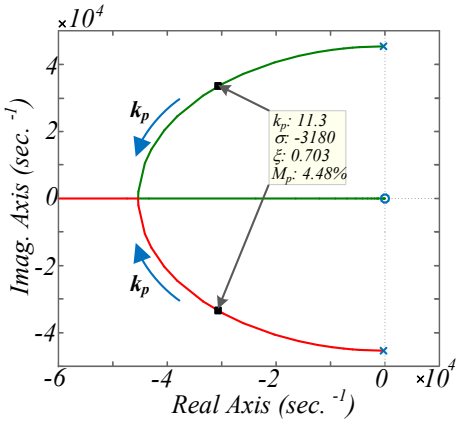

Fig. 3. Root locus for the inner current loop with P regulator, without voltage decoupling and neglecting system delays: x – open loop poles; ■ closed-loop poles for $\boldsymbol{k_{pI} = 11.32}$; o – zeros

By taking into account system delays in (2) and looking just at the command tracking features, the root locus is shown in Fig. 4. It can be seen that if the states are not decoupled the system has low damping and hence high overshoot. This is true whatever gain is selected.

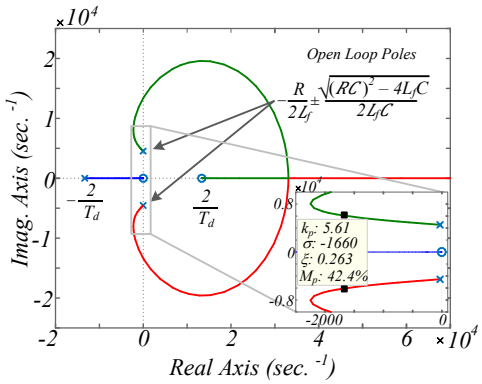

Fig. 4. Root locus for the inner current loop with P regulator and without voltage decoupling: x – open loop poles; ■ closed-loop poles for $\boldsymbol{k_{pI} = 5.61}$; o – zeros

In order to analyze the effect of decoupling the controlled states, an ideal case is discussed, i.e. ideal voltage decoupling is considered. This corresponds to consider $G_{dec}(s) = G_{PWM}(s)^{-1}$. The system becomes second order and higher damping is achieved with less overshoot for the same bandwidth, as shown in the root locus of Fig. 5. Equation (1) is modified accordingly

$$\frac{\boldsymbol{I}_{L\alpha\beta}(s)}{\boldsymbol{I}^*_{L\alpha\beta}(s)} = \frac{G_i(s)G_{PWM}(s)}{L_f s + R + G_i(s)G_{PWM}(s)}. \tag{3}$$

By observing this TF, it is possible to conclude that the output current does not affect anymore the inner current loop. This result is an easier design of the controller, with better dynamics, and with a dynamic behavior that is not load sensitive.

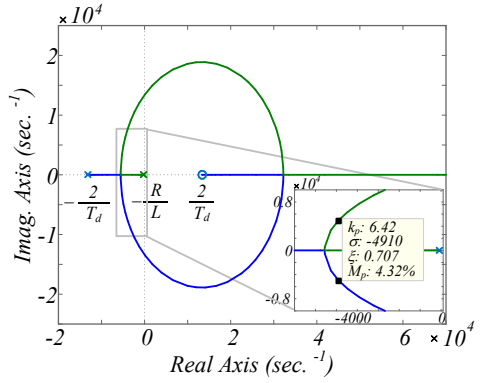

Fig. 5. Root locus for the inner current loop with P regulator and ideal voltage decoupling: x – open loop poles; ■ closed-loop poles for $\boldsymbol{k_{pI} = 6.42}$; o – zeros

However, this corresponds to design $G_{dec}(s) = G_{PWM}(s)^{-1}$, which results in an unstable TF if the approximation for $G_{PWM}(s)$ with the non-minimum phase zero is used.

If $G_{dec}(s) = 1$, the computation and PWM delays on the state feedback decoupling path are not compensated. Compared to ideal voltage decoupling the damping of the system degrades (see Fig. 6) for the same proportional gain. However, the damping is still much higher than without voltage decoupling.

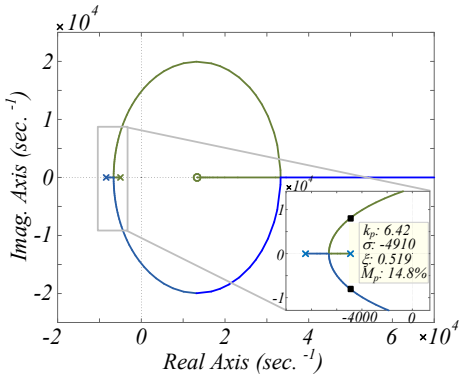

Fig. 6. Root locus for the inner current loop with P regulator and non-ideal voltage decoupling [$\boldsymbol{G_{dec}(s) = 1}$]: x – open loop poles; ■ closed-loop poles for $\boldsymbol{k_{pI} = 6.42}$; o – zeros

If the controlled states are not decoupled the system is load dependent. To highlight this issue, the effect of $\boldsymbol{I}_{o\alpha\beta}(s)$ as a function of the output voltage and a generic load impedance $\boldsymbol{Z}(s)$ is introduced ($\boldsymbol{I}_{o\alpha\beta}(s) = \boldsymbol{V}_{c\alpha\beta}(s)/\boldsymbol{Z}(s)$). It is thus possible to derive in just one TF the steady state features of tracking and disturbance. The following model can be employed

$$\frac{\boldsymbol{I}_{o\alpha\beta}(s)}{\boldsymbol{I}_{L\alpha\beta}(s)} = \frac{1}{\boldsymbol{Z}(s)C_f s + 1}. \tag{4}$$

Substituting (4) in (1) with $G_{dec}(s) = 0$, i.e. without decoupling the states, leads to the closed loop TF

$$\frac{\boldsymbol{I}_{L\alpha\beta}(s)}{\boldsymbol{I}^*_{L\alpha\beta}(s)} = \frac{\boldsymbol{Z}(s)C_f^2 G_i(s)G_{PWM}(s)s + G_i(s)G_{PWM}(s)C_f}{a_2 s^2 + b_2 s + c_2}, \tag{5}$$

being

$$a_2 = \boldsymbol{Z}(s)L_f C_f^2,$$

$$b_2 = \boldsymbol{Z}(s)RC_f^2 + \boldsymbol{Z}(s)C_f^2 G_i(s)G_{PWM}(s) + L_f C_f,$$

$$c_2 = \boldsymbol{Z}(s)C_f + RC_f + G_i(s)G_{PWM}(s)C_f.$$

On the other hand, by substituting (4) in (1) and decoupling the states with $G_{dec}(s) = 1$, leads to the closed loop TF for the current loop

$$\frac{\boldsymbol{I}_{L\alpha\beta}(s)}{\boldsymbol{I}^*_{L\alpha\beta}(s)} = \frac{\boldsymbol{Z}(s)C_f^2 G_i(s)G_{PWM}(s)s + G_i(s)G_{PWM}(s)C_f}{a_2 s^2 + b_2 s + c_3}, \tag{6}$$

being

$$c_3 = \boldsymbol{Z}(s)C_f + RC_f + G_i(s)G_{PWM}(s)C_f - \boldsymbol{Z}(s)G_{PWM}(s)C_f.$$

The frequency response (FR) analysis of the current loop based on (3) and (5) are shown in Fig. 7. The arrow indicates increase in the load impedance, from rated load to open-circuit conditions. For any value of the impedance the system shows a low gain for a broad frequency range including fundamental frequency (50 Hz), which means the command reference is not properly tracked resulting in high steady-state error. On the other hand, if ideal voltage decoupling is performed, the system becomes not dependent on the load impedance and

almost zero steady-state error can be achieved even with a simple P controller. It must be remarked this low steady-state error depends on the value of the inductor ESR.

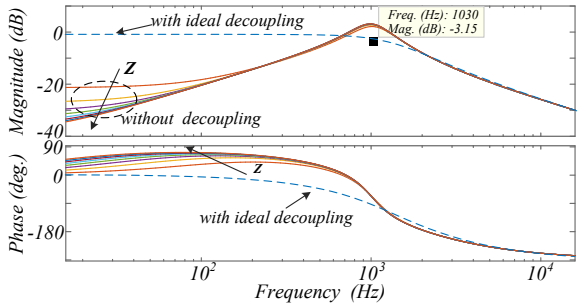

Fig. 7. Closed-loop FR analysis for the inner current loop with P regulator and with ideal and without voltage decoupling – arrows indicate decreasing in load (from rated resistive load until no-load)

The FR of the current loop based on (6) is shown in Fig. 8. If non-ideal voltage decoupling with $G_{dec}(s) = 1$ is performed, the system is still load dependent, but to a much lesser extent than without decoupling the controlled states.

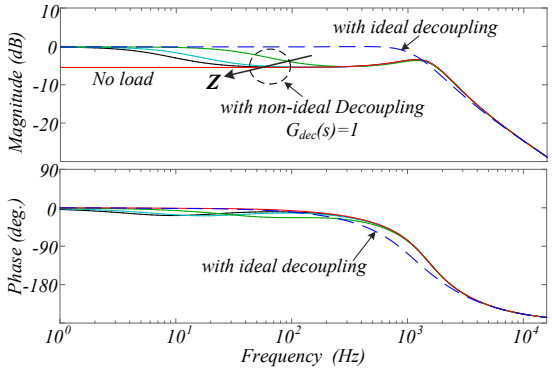

Fig. 8. Closed-loop FR for the inner current loop with P regulator and with non-ideal $[\boldsymbol{G_{dec}(s) = 1}]$ and ideal voltage decoupling – arrows indicate decreasing in load (from rated resistive load until no-load)

IV. Voltage Regulator Design

The voltage regulator is based on PR controllers with a lead compensator structure

$$G_v(s) = k_{pV} + \sum_{h=1,5,7} k_{iV,h} \frac{s\cos(\varphi_h) - h\omega_1 \sin(\varphi_h)}{s^2 + (h\omega_1)^2}. \quad (7)$$

The gains of the system are selected to provide a good dynamics response when the system is tested according to the requirements imposed by the standard for islanded systems. The proportional gain k_{pV} determines the bandwidth of the voltage regulator, and is designed for around 150 Hz. The leading angles φ_h at each harmonic frequency are set such that the trajectories of the open loop system on the Nyquist diagram, with the PR regulators at fundamental, 5th and 7th harmonics, guarantee a sensitivity function η higher than a threshold value [10]. In this work this threshold has been set to $\eta = 0.5$ at no-load condition. After calculating the phase-leading angles, the fundamental resonant gain $k_{iV,1}$ is selected in order to have a fast response to changes in the fundamental component. Equation (7) can be rearranged, leading to the second-order system

$$G_v(s) = k_{pV} \frac{s^2 + \frac{k_{iV,1}}{k_{pV}}\cos(\varphi_1)s + \left[\omega_1^2 - \frac{k_{iV,1}}{k_{pV}}\omega_1 \sin(\varphi_1)\right]}{s^2 + \omega_1^2}. \quad (8)$$

According to Evans root locus theory, the open loop poles move towards the open loop zeros when the loop is closed. For this reason, the pair of zeros of the PR controller are moved as furthest as possible from the right half plane. This corresponds to place them on the same location, such that the pair of poles of $G_v(s)$ are coincident. This corresponds to design $k_{iV,1}$ according to

$$k_{iV,1} \geq K \frac{2k_{pV}\zeta_{crit}\omega_1}{\cos(\varphi_1)}, \quad (9)$$

where the lower bound of the inequality refers to $K = 1$, with the damping factor $\zeta_{crit} = 1$. For the leading angle at fundamental frequency $\varphi_1 = 3.3°$, the gain is $k_{iV,1} = 31.47$. The upper bound is set by $k_{iV,1}$ values which do not significantly degrade the relative stability of the closed-loop system [2]. The harmonic resonant gains are selected to have reduced transient oscillations [7], as well as to fulfill the requirements set by the UPS standards (see Table III).

The leading angles in (7) are selected with the goal to compensate for the discrete time delay at each specific harmonic. According to [10], an accurate approximation for each leading angle is given by

$$\varphi_h = \frac{3}{2} h\omega_1 T_s, \quad (10)$$

Subsequently, a fine tuning is provided by the inspection of the Nyquist diagrams at no load and rated load conditions. The goal of each φ_h is to maximize the sensitivity peaks corresponding to the resonant frequencies; i.e. to place the Nyquist trajectory as far as possible from the (-1,0j) point.

TABLE III
Voltage Regulator Control Parameters

Parameter		Value	
Proportional gain		$k_{pV} = 0.05$	
Integral gains and leading angles	@50Hz	$k_{iV,1} = 31.47$	$\varphi_1 = 3.3°$
	@250Hz	$k_{iV,5} = 15$	$\varphi_5 = 37°$
	@350Hz	$k_{iV,7} = 15$	$\varphi_7 = 44°$

The system in Fig. 2 can be simplified for design purposes, as shown in Fig. 9.

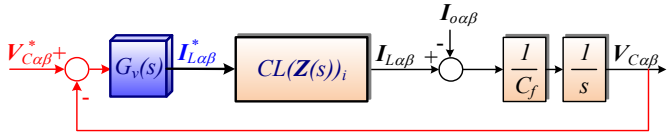

Fig. 9. Block diagram for the outer voltage loop design using ideal voltage decoupling. Simplification of Fig. 2

The closed-loop TF for the current loop $CL(\boldsymbol{Z}(s))_i$ has the form of (6) if the states are decoupled with $G_{dec}(s) = 1$.

In Fig. 10 the Nyquist diagram of the system in Fig. 7 with the parameters of Table III is shown. The correspondent open-loop TF (command tracking only) is

$$\frac{\boldsymbol{V}_{c\alpha\beta}(s)}{\boldsymbol{V}^{*}_{c\alpha\beta}(s)} = G_v(s)\frac{CL\big(\boldsymbol{Z}(s)\big)_i}{C_f s}. \tag{10}$$

The sensitivity function is higher than 0.5 at no-load condition and 0.4 at rated load ($Z = 68\ \Omega$), respectively.

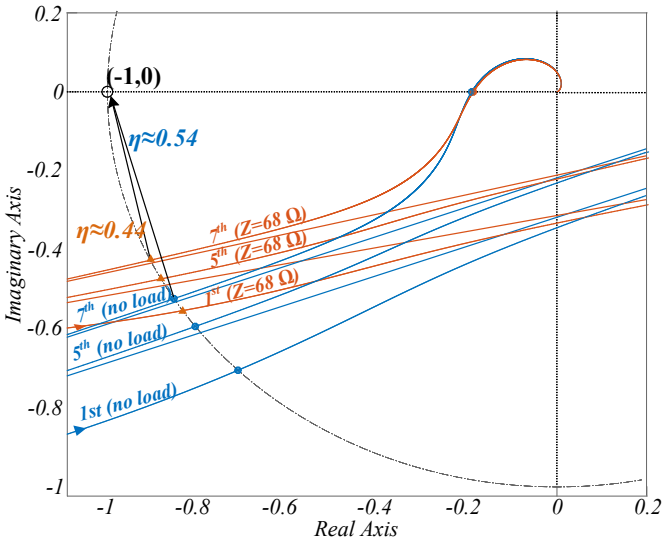

Fig. 10. Nyquist diagram of the system at no-load and rated load ($\boldsymbol{Z} = \mathbf{68}\ \Omega$) conditions

V. Experimental Results

The power system of Fig. 1 was tested to check the theoretical analysis presented. For this purpose, a low scale test-bed has been built using a Danfoss 2.2 kW converter, driven by a dSpace DS1006 platform. The filter parameters and operational information are presented in Table I. The implementation of the regulators is made in the discrete time domain using Impulse Invariant as discretization method for the resonant terms.

Regarding the current loop only, a step response is performed. Without voltage decoupling, because of the low gain at low frequencies (see Fig. 7) a high reference current must be provided to achieve the rated current value. However, as the initial current was too high, the converter protections activate. In order to obtain step response captures without voltage decoupling, a lower reference current is provided. In Fig. 11 it can be seen the current during the transient is higher than the steady-state value because of low damping. It should be noted the different scales for the reference (50 A/div) and real inductor current in α-axis (5 A/div). This test proves that the current loop is not working properly, since the reference is not tracked. With reference to voltage decoupling the response is much more damped and the reference current is in the order of magnitude of the real current (Fig. 12). It can be stated that a simple P controller can be used in the current loop, only if voltage decoupling is performed.

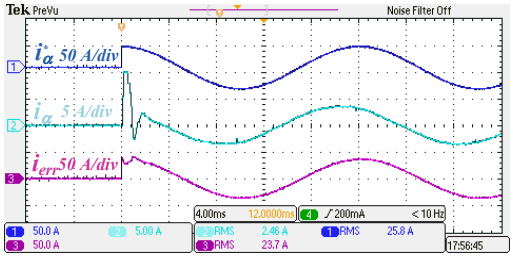

Fig. 11. Step response of the reference current without voltage decoupling: (1) reference; (2) real; (3) inductor current error - (α-axis), time scale (4 ms /div)

With reference to voltage decoupling with $G_{dec}(s) = 1$ the response is much more damped and the steady-state error is almost zero, even if just a P controller is used (see Fig. 12).

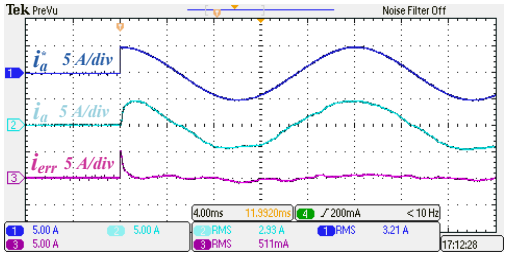

Fig. 12. Step response of the reference current with voltage decoupling and $\boldsymbol{G_{dec}(s) = 1}$: (1) reference; (2) real; (3) inductor current error - (α-axis), time scale (4 ms/div)

All the following results (from Fig. 13 to Fig. 16) including the voltage loop are obtained with voltage decoupling and a P controller as current regulator.

In Fig. 13(a) a 100% linear (resistive) step load change is shown. The results obtained are compared to the envelope of the voltage deviation v_{dev} as reported in the IEC 62040 standard for UPS systems [see Fig. 13(b)]. It can be seen that the system reaches steady-state in less than half a cycle after the load step change. The dynamics response is within the limits imposed by the standard.

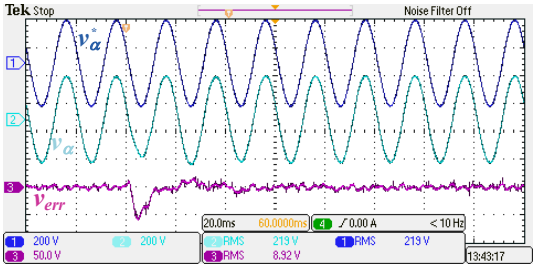

(a)

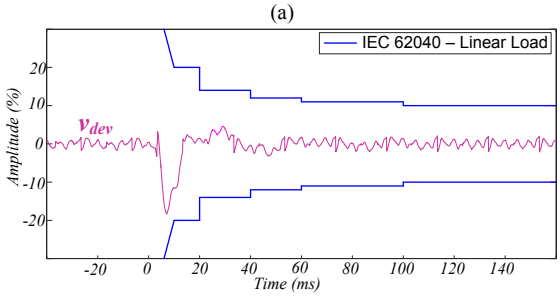

(b)

Fig. 13. Linear step load changing (0 – 100%): (a) reference (200 V/div), real (200 V/div), and capacitor voltage error (50 V/div) (α-axis), time scale (20 ms/div); (b) Dynamic characteristics according to IEC 62040 standard for linear loads

A diode bridge rectifier with an LC output filter supplying a resistive load is used as non-linear load. Its parameters are presented in Table I.

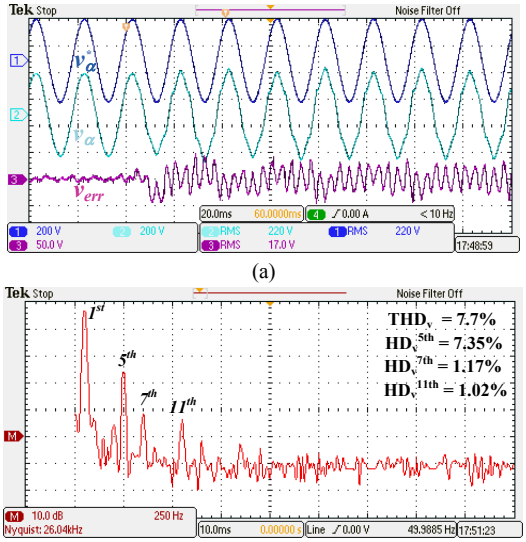

Fig. 14. Voltage loop without HC and nonlinear load: (a) 100% Step load change, reference (200 V/div), real (200 V/div), and capacitor voltage error (50 V/div) (α-axis), time scale (20 ms/div); (b) FFT of the capacitor voltage (250 Hz/div)

A 100% non-linear step load change is performed without and with harmonic compensators (HC) tuned only at 5^{th} and then at 5^{th} and 7^{th} harmonics (see Fig. 14, Fig. 15, and Fig. 16).

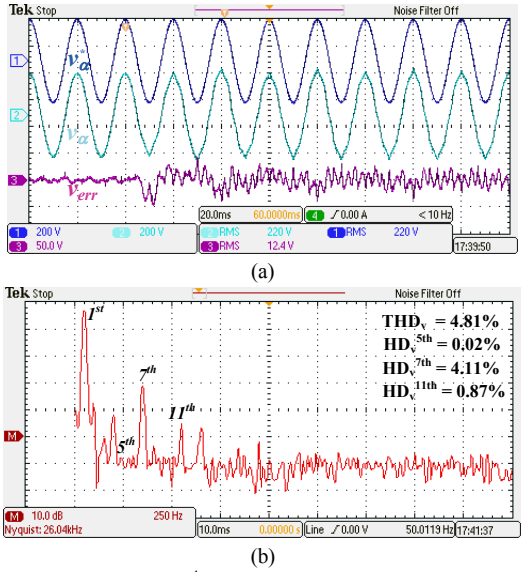

Fig. 15. Voltage loop with 5^{th} HC and nonlinear load: (a) 100% Step load change, reference (200 V/div), real (200 V/div), and capacitor voltage error (50 V/div) (α-axis), time scale (20 ms/div); (b) FFT of the capacitor voltage (250 Hz/div)

The results with all the HC activated are in accordance with the IEC 62040 standard [see Fig. 16(c)], even for linear loads.

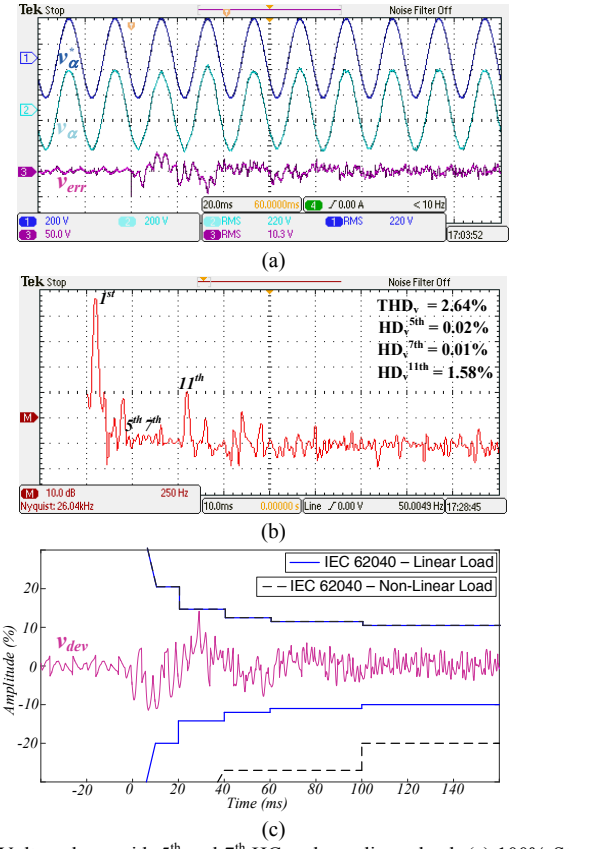

Fig. 16. Voltage loop with 5^{th} and 7^{th} HC and non-linear load: (a) 100% Step load change, reference (200 V/div), real (200 V/div), and capacitor voltage error (50 V/div) (α-axis), time scale (20 ms/div); (b) FFT of the capacitor voltage (250 Hz/div); (c) Dynamic characteristics according to IEC 62040 standard for linear and non-linear loads

From the comparison of the FFT analysis in Fig. 14(b) and Fig. 16(b) it can be clearly seen the compensation of the harmonics to which the resonant controllers have been tuned. However, some small amplification of higher order harmonics can be observed in the frequency spectrum, in particular the 11^{th} harmonic. This is expected as the resonant peaks can slightly affect neighbors.

VI. Conclusions

In standalone microgrids the decoupling of the controlled states allows to achieve a more damped system along with less overshoot. The computation and PWM delays limit the maximum bandwidth that can be achieved by the current regulator. The dynamics of the system does not depend on the load when ideal capacitor voltage decoupling is performed, allowing even a proportional controller to be used as current regulator. However, decoupling ideally the controlled states is not feasible. The system is thus still dependent on the load but to a much lesser extent than without decoupling.

Since the design is based on serial tuning, the current loop design is followed by the voltage regulator tuning. A criterion based on moving the zeros of the controller on the real-axis has been proposed to determine the minimum value of the integral gain at fundamental. Inspection of the open loop trajectories on the Nyquist diagram along with the fulfillment

of the demanding requirements imposed by UPS standards, allow to determine the leading angles and resonant gains values at different harmonic orders.

ACKNOWLEDGEMENT

This work was supported in part by the National Natural Science Foundation of Brazil - CNPq, Schneider Electric/Brazil, and CEMAR.

REFERENCES

[1] J. C. Vasquez, J. M. Guerrero, M. Savaghebi, J. Eloy-Garcia, and R. Teodorescu, "Modeling, Analysis, and Design of Stationary-Reference-Frame Droop-Controlled Parallel Three-Phase Voltage Source Inverters," *IEEE Trans. Ind. Electron.,* vol. 60, pp. 1271-1280, 2013.

[2] K. Hongrae, M. W. Degner, J. M. Guerrero, F. Briz, and R. D. Lorenz, "Discrete-Time Current Regulator Design for AC Machine Drives," *IEEE Trans. Ind. Appl.,* vol. 46, pp. 1425-1435, 2010.

[3] R. Teodorescu, M. Liserre, and P. Rodriguez, *Grid Converters for Photovoltaic and Wind Power Systems*: Wiley-IEEE Press, 2011.

[4] F. de Bosio, L. A. de S. Ribeiro, M. S. Lima, F. D. Freijedo, J. M. Guerrero, and M. Pastorelli, "Current control loop design and analysis based on resonant regulators for microgrid applications," in *IEEE Conf. Rec. IECON*, Yokohama, Japan, 2015, pp. 5322 - 5327.

[5] D. G. Holmes, T. A. Lipo, B. P. McGrath, and W. Y. Kong, "Optimized Design of Stationary Frame Three Phase AC Current Regulators," *IEEE Trans. Power Electron.,* vol. 24, pp. 2417-2426, 2009.

[6] P. C. Loh and D. G. Holmes, "Analysis of multiloop control strategies for LC/CL/LCL-filtered voltage-source and current-source inverters," *IEEE Trans. Ind. Appl.,* vol. 41, pp. 644-654, 2005.

[7] A. Vidal, F. D. Freijedo, A. G. Yepes, P. Fernández-Comesaña, J. Malvar, O. López*, et al.*, "Assessment and Optimization of the Transient Response of Proportional-Resonant Current Controllers for Distributed Power Generation Systems," *IEEE Trans. Ind. Electron.,* vol. 60, pp. 1367-1383, 2013.

[8] S. S. H. Bukhari, T. A. Lipo, and B. Kwon, "An on-line UPS system that eliminates the inrush current phenomenon while feeding multiple load transformers," in *IEEE Conf. Rec. ICPE-ECCE Asia*, Seoul, Korea, 2015, pp. 385-390.

[9] F. Briz, M. W. Degner, and R. D. Lorenz, "Analysis and design of current regulators using complex vectors," *IEEE Trans. Ind. Appl.,* vol. 36, pp. 817-825, 2000.

[10] A. G. Yepes, F. D. Freijedo, O. López, and J. Doval-Gandoy, "Analysis and Design of Resonant Current Controllers for Voltage-Source Converters by Means of Nyquist Diagrams and Sensitivity Function," *IEEE Trans. Ind. Electron.,* vol. 58, pp. 5231-5250, 2011.